# Validation of a fully automated 3D hippocampal segmentation method using subjects with Alzheimer's disease mild cognitive impairment, and elderly controls

Jonathan H. Morra [a], Zhuowen Tu [a], Liana G. Apostolova [a,b], Amity E. Green [a,b], Christina Avedissian [a], Sarah K. Madsen [a], Neelroop Parikshak [a], Xue Hua [a], Arthur W. Toga [a], Clifford R. Jack Jr. [c], Michael W. Weiner [d,e], Paul M. Thompson [a,*]
The Alzheimer's Disease Neuroimaging Initiative [1]

[a] Laboratory of Neuro Imaging, Department of Neurology, UCLA School of Medicine, Los Angeles, CA, USA
[b] Department of Neurology, UCLA School of Medicine, Los Angeles, CA, USA
[c] Mayo Clinic College of Medicine, Rochester, MN, USA
[d] Department of Radiology, UC San Francisco, San Francisco, CA, USA
[e] Department of Medicine and Psychiatry, UC San Francisco, San Francisco, CA, USA

## ARTICLE INFO

## ABSTRACT

We introduce a new method for brain MRI segmentation, called the auto context model (ACM), to segment the hippocampus automatically in 3D T1-weighted structural brain MRI scans of subjects from the Alzheimer's Disease Neuroimaging Initiative (ADNI). In a training phase, our algorithm used 21 hand-labeled segmentations to learn a classification rule for hippocampal versus non-hippocampal regions using a modified AdaBoost method, based on ~18,000 features (image intensity, position, image curvatures, image gradients, tissue classification maps of gray/white matter and CSF, and mean, standard deviation, and Haar filters of size $1 \times 1 \times 1$ to $7 \times 7 \times 7$). We linearly registered all brains to a standard template to devise a basic shape prior to capture the global shape of the hippocampus, defined as the pointwise summation of all the training masks. We also included curvature, gradient, mean, standard deviation, and Haar filters of the shape prior and the tissue classified images as features. During each iteration of ACM – our extension of AdaBoost – the Bayesian posterior distribution of the labeling was fed back in as an input, along with its neighborhood features as new features for AdaBoost to use. In validation studies, we compared our results with hand-labeled segmentations by two experts. Using a leave-one-out approach and standard overlap and distance error metrics, our automated segmentations agreed well with human raters; any differences were comparable to differences between trained human raters. Our error metrics compare favorably with those previously reported for other automated hippocampal segmentations, suggesting the utility of the approach for large-scale studies.

Published by Elsevier Inc.

## Introduction

Alzheimer's disease (AD) is the most common type of dementia, and affects over 5 million people in the United States alone (Jorm et al., 1987). The disease is associated with the pathological accumulation of amyloid plaques and neurofibrillary tangles in the brain, and first affects memory systems, progressing to involve language, affect, exe-

cutive function, and all aspects of behavior. A major therapeutic goal is to assess whether treatments delay or resist disease progression in the brain before widespread cortical and subcortical damage occurs. For this, sensitive neuroimaging measures have been sought to quantify structural changes in the brain in early AD which are automated enough to permit large-scale studies of disease and the factors that affect it.

To track the disease process, several MRI- or PET-based imaging measures have been proposed. Many studies have sought optimal volumetric measures (e.g., of the hippocampus or entorhinal cortex) to differentiate normal aging from AD, and from mild cognitive impairment (MCI), a transitional state that carries a 4–6 fold increased risk of imminent decline to AD relative to the normal population (Petersen, 2000; Petersen et al., 1999, 2001). A common biological marker of disease progression is morphological change in the hippocampus, assessed using volumetric measures (Jack et al., 1999;

Kantarci and Jack, 2003) or by mapping the spatial distribution of atrophy in 3D (Apostolova et al., 2006a,b; Csernansky et al., 1998; Frisoni et al., 2006; Thompson et al., 2004).

Using MRI at millimeter resolution, subtle hippocampal shape changes may be resolved. However, isolating the hippocampus in a large number of MRI scans is time-consuming, and most studies still rely on manual outlining guided by expert knowledge of the location and shape of each region of interest (ROI) (Apostolova et al., 2006a; Du et al., 2001). To accelerate epidemiological studies and clinical trials, this process should be automated. Some automated systems have been proposed for hippocampal segmentation (Barnes et al., 2004; Crum et al., 2001; Fischl et al., 2002; Hogan et al., 2000; Powell et al., 2008; Wang et al., 2007; Yushkevich et al., 2006), but none is yet widely used.

Pattern recognition techniques (Duda et al., 2001) offer a range of promising algorithms for automated subcortical segmentation. Most pattern recognition (or machine learning) algorithms attempt to assign a probability to a specific outcome. In image segmentation, image cues are pooled to determine with a specific probability whether each image voxel is part of an ROI (e.g., the hippocampus) or not. In pattern recognition, cues are usually referred to as features, and different pattern recognition algorithms combine these features in different ways. When using pattern recognition approaches, it is standard practice to divide a dataset into two non-overlapping classes for training and testing. The training set is used to learn the patterns (e.g., estimate a function or decision rule for classifying voxels), and the testing set is used to validate how well new datasets can be classified, based on the patterns that were learned.

Since medical images are complex, many possible features may be created to represent each voxel. Given the large number of voxels in an MRI scan, computing and storing this amount of data may become unmanageable. For example, features may consist of image intensity, $x$, $y$, and $z$ positions, image curvature, image gradients, or the output of any other general image filter. To overcome this problem, we use a variant of a machine learning algorithm called AdaBoost (Freund and Schapire, 1997). AdaBoost is a weighted voting algorithm, which combines "weak learners" into a "strong learner." A weak learner is any pattern recognition algorithm that guesses correctly greater than half of the time. At each iteration, AdaBoost selects a weak learner that minimizes the error for all voxels based on the classification of previously selected weak learners. Therefore, an incorrectly classified example at one iteration will receive more weight on subsequent iterations.

To segment the hippocampus in an MRI scan, we use AdaBoost inside a new pattern recognition algorithm we call the auto context model (ACM). ACM is not specific to AdaBoost and may be used with any classification technique, but here we use it with AdaBoost, which has previously been found to be effective for subcortical segmentation in smaller samples of subjects (Morra et al., 2007; Quddus et al., 2005; Tu et al., 2008).

This paper presents a validation study of ACM using data from an Alzheimer's disease study. We show that this approach accurately captures the hippocampus and may therefore be useful in large-scale studies of AD where manual tracing would be prohibitive.

## Methods

### Subjects

The Alzheimer's Disease Neuroimaging Initiative (ADNI) (Mueller et al., 2005a,b) is a large multi-site longitudinal MRI and FDG-PET (fluorodeoxyglucose positron emission tomography) study of 800 adults, ages 55 to 90, including 200 elderly controls, 400 subjects with mild cognitive impairment, and 200 patients with AD. The ADNI was launched in 2003 by the National Institute on Aging (NIA), the National Institute of Biomedical Imaging and Bioengineering (NIBIB), the Food and Drug Administration (FDA), private pharmaceutical companies and non-profit organizations, as a $60 million, 5-

year public–private partnership. The primary goal of ADNI has been to test whether serial MRI, PET, other biological markers, and clinical and neuropsychological assessment can be combined to measure the progression of MCI and early AD. Determination of sensitive and specific markers of very early AD progression is intended to aid researchers and clinicians to develop new treatments and monitor their effectiveness, as well as lessen the time and cost of clinical trials. The Principal Investigator of this initiative is Michael W. Weiner, M.D., VA Medical Center and University of California, San Francisco.

All subjects underwent thorough clinical/cognitive assessment at the time of scan acquisition. As part of each subject's cognitive evaluation, the Mini-Mental State Examination (MMSE) was administered to provide a global measure of cognitive status based on evaluation of five cognitive domains (Cockrell and Folstein, 1988; Folstein et al., 1975); scores of 24 or less (out of a maximum of 30) are generally consistent with dementia. Two versions of the Clinical Dementia Rating (CDR) were also used as a measure of dementia severity (Hughes et al., 1982; Morris, 1993). The global CDR represents the overall level of dementia, and a global CDR of 0, 0.5, 1, 2 and 3, respectively, indicate no dementia, very mild, mild, moderate, or severe dementia. The "sum-of-boxes" CDR score is the sum of 6 scores assessing different areas of cognitive function: memory, orientation, judgment and problem solving, community affairs, home and hobbies, and personal care. The sum of these scores ranges from 0 (no dementia) to 18 (very severe dementia). Table 1 shows the clinical scores and demographic measures for our sample. The elderly normal subjects in our sample had MMSE scores between 26 and 30, a global CDR of 0, a sum-of-boxes CDR between 0 and 0.5, and no other signs of MCI or other forms of dementia. The MCI subjects had MMSE scores ranging from 24 to 30, a global CDR of 0.5, a sum-of-boxes CDR score between 0.5 and 5, and mild memory complaints. Memory impairment was assessed via education-adjusted scores on the Wechsler Memory Scale — Logical Memory II (Wechsler, 1987). All AD patients met NINCDS/ADRDA criteria for probable AD (McKhann et al., 1984) with an MMSE score between 20 and 26, a global CDR between 0.5 and 1, and a sum-of-boxes CDR between 1.0 and 9.0. As such, these subjects would be considered as having mild, but not severe, AD. Detailed exclusion criteria, e.g., regarding concurrent use of psychoactive medications, may be found in the ADNI protocol (page 29, http://www.adni-info.org/images/stories/Documentation/adni_protocol_03.02.2005_ss.pdf). Briefly, subjects were excluded if they had any serious neurological disease other than incipient AD, any history of brain lesions or head trauma, or psychoactive medication use (including antidepressants, neuroleptics, chronic anxiolytics or sedative hypnotics, etc.).

The study was conducted according to Good Clinical Practice, the Declaration of Helsinki and U.S. 21 CFR Part 50-Protection of Human Subjects, and Part 56-Institutional Review Boards. Written informed consent for the study was obtained from all participants before protocol-specific procedures, including cognitive testing, were performed.

**Table 1**
Demographic data and clinical scores are shown for the subjects whose scans were analyzed in this paper

|  | N | Males/females | Age (years) | MMSE | Global CDR | Sum-of-boxes CDR |
|---|---|---|---|---|---|---|
| Normal | 7 | 4/3 | 67.45 (3.71) | 29.00 (0.82) | 0 (0) | 0.071 (0.19) |
| MCI | 7 | 4/3 | 67.47 (2.43) | 27.28 (1.38)** | 0.5 (0)** | 1.71 (0.91)** |
| AD | 7 | 3/4 | 68.14 (2.44) | 22.29 (0.76)** | 0.57 (0.19)** | 3.57 (1.4)** |

Means are shown with standard deviations in parentheses. This data is provided to show that our individuals encompassed a wide variety of cognitive impairment. Throughout the paper, $p$-values for group differences were obtained from two sided $t$-tests.
** $p < 0.01$.

*Training and testing set descriptions*

As noted earlier, when using a pattern recognition approach to identify structures in images, two non-overlapping sets of images must be defined, for training and testing (Morra et al., 2007; Powell et al., 2008). The training set consists of a small sample of brain images, representative of the entire dataset, which are manually traced by experts. The testing set is a group of brain images that are to be segmented by the algorithm, but have not been used for training the algorithm. Our training set consisted of 21 brain images, from 7 healthy elderly individuals, 7 individuals with MCI, and 7 individuals with AD. Since we only have manual tracings of these brains, we construct our testing set using a leave-one-out approach. For testing, we train 21 models, each one ignoring one subject (i.e., not using that subject for training), and we then test each model on the subject that it ignored. This gives a testing set of the same 21 brains, each with a ground truth segmentation for comparison purposes; even so, it ensures the independence of the training and testing sets, a common requirement in validating machine learning methods. We chose to train on 21 subjects because this number was sufficient in previous studies that varied the training sample size (Morra et al., 2007); smaller training sets degraded segmentation performance. Each of the three groups (AD, MCI, and controls) were age- and gender-matched as closely as possible as shown in Table 1.

*MRI acquisition and pre-processing*

All subjects were scanned with a standardized MRI protocol, developed after a major effort evaluating and comparing 3D T1-weighted sequences for morphometric analyses (Jack et al., 2008; Leow et al., 2006).

High-resolution structural brain MRI scans were acquired at multiple ADNI sites using 1.5 T MRI scanners manufactured by General Electric Healthcare and Siemens Medical Solutions. ADNI also collects data at 3.0 T from a subset of subjects, but to avoid having to model field strength effects in this initial study, only 1.5 T images were used. All scans were collected according to the standard ADNI MRI protocol (http://www.loni. ucla.edu/ADNI/Research/Cores/index.shtml). For each subject, two T1-weighted MRI scans were collected using a sagittal 3D MP-RAGE sequence. Typical 1.5 T acquisition parameters are repetition time (TR) of 2400 ms, minimum full excitation time (TE), inversion time (TI) of 1000 ms, flip angle of 8°, 24 cm field of view, acquisition matrix was $192 \times 192 \times 166$ in the *x*-, *y*-, and *z*-dimensions yielding a voxel size of $1.25 \times 1.25 \times 1.2$ mm$^3$ (Jack et al., 2008). In plane, zero-filled reconstruction yielded a $256 \times 256$ matrix for a reconstructed voxel size of $0.9375 \times 0.9375 \times 1.2$ mm$^3$. The ADNI MRI quality control center at the Mayo Clinic (in Rochester, MN, USA) selected the MP-RAGE image with higher quality based on standardized criteria (Jack et al., 2008). Additional phantom-based geometric corrections were applied to ensure spatial calibration was kept within a specific tolerance level for each scanner involved in the ADNI study (Gunter et al., 2006).

Additional image corrections were also applied, using a processing pipeline at the Mayo Clinic, consisting of: (1) a procedure termed *GradWarp* for correction of geometric distortion due to gradient non-linearity (Jovicich et al., 2006), (2) a "B1-correction", to adjust for image intensity non-uniformity using B1 calibration scans (Jack et al., 2008), (3) "N3" bias field correction, for reducing intensity inhomogeneity (Sled et al., 1998), and (4) geometrical scaling, according to a phantom scan acquired for each subject (Jack et al., 2008), to adjust for scanner- and session-specific calibration errors. In addition to the original uncorrected image files, images with all of these corrections already applied (*GradWarp*, B1, phantom scaling, and N3) are available to the general scientific community, as described at http://www.loni.ucla.edu/ADNI. Ongoing studies are examining the influence of N3 parameter settings on measures obtained from ADNI scans (Boyes et al., 2008).

*Image pre-processing*

To adjust for global differences in brain positioning and scale across individuals, all scans were linearly registered to the stereotactic space defined by the International Consortium for Brain Mapping (ICBM-53) (Mazziotta et al., 2001) with a 9-parameter (9P) transformation (3 translations, 3 rotations, 3 scales) using the Minctracc algorithm (Collins et al., 1994). Globally aligned images were resampled in an isotropic space of 220 voxels along each axis (*x*, *y*, and *z*) with a final voxel size of 1 mm$^3$.

*Feature selection*

All discriminative pattern recognition techniques involve taking some set of examples with a label and learning a pattern based on those examples. Usually the examples are themselves each a vector of problem-specific information, referred to as features. Each feature must be calculable for each example (for implementation purposes, hopefully quickly), and the features should provide some insight into the classification task. For medical image segmentation, these features are derived at each voxel in all brains, so at each voxel, there exists a vector for which each entry is a specific feature evaluated at that voxel.

In our case, we chose features based on image intensity, tissue classification maps of gray matter, white matter, and CSF (maps obtained by an unsupervised classifier, PVC (*partial volume classifier*; (Shattuck et al., 2001))) and neighborhood-based features derived from the tissue classified maps, *x*, *y*, and *z* positions (along with combinations of positions such as $x+y$ or $x*z$), curvature filters, gradient filters, mean filters, standard deviation filters, and Haar filters (Viola and Jones, 2004) of sizes varying from $1 \times 1 \times 1$ to $7 \times 7 \times 7$.*x*, *y*, *z* positions were determined using stereotaxic coordinates after spatial normalization to the standard space. In addition to these features, we exploited the fact that all the brains had been registered to devise a basic shape prior to capture the global shape of the hippocampus. Our shape prior was defined as the pointwise summation of all the training masks. Differential positional effects in the *x*, *y*, and *z* positions are therefore captured by using a shape prior, and also by including products of *x*, *y*, and *z* voxel indices as features.

Since brain MRIs consist of many voxels, the product of the number of features and the number of voxels can be exceedingly large. However, because all of our brains are registered to the same template, the hippocampi will always appear in approximately the same localized region. We can exploit this fact to reduce our search space by constructing a bounding box, and only classifying examples (feature vectors at each voxel) for voxels that fall in this bounding box. To define the box we scan over all the training examples and find the minimum and maximum *x*, *y*, *z* positions of the hippocampus. Next, we add the size of the largest neighborhood feature (in this case, 7 voxels) and some additional voxels to cope with as yet unseen testing brains (in this case, 10 voxels). Then training commences on only voxels inside of this box. Also, when testing a new brain, only voxels inside this box are classified, all others are assumed negative. All features are computed at each voxel, rather than averaging them over the bounding box. When classifying each voxel, features such as image intensity, image gradient, and tissue classification are computed voxel-wise. The number of features is approximately 18,000 per voxel, and the same set of candidate features are available to the classifier at every voxel, so the number of features does not depend on the size of the bounding box.

*AdaBoost description*

AdaBoost is a machine learning method that uses a training set of data to develop rules for classifying future data; it combines individual rules that do not work especially well into a pool of rules that can be used to more accurately classify new data. The overall classifier can greatly outperform the component classifiers. The component

classifiers are often called "weak learners," as they may perform only slightly better than random; for example, a classifier of hippocampal voxels based on the binary feature "voxel is gray matter" could classify the hippocampus only slightly better than chance (i.e., 50% correct), as there are many non-hippocampal gray matter voxels. AdaBoost iteratively selects weak learners, $h(x)$, from a candidate pool and combines them into a strong learner, $H(x)$ (Freund and Schapire, 1997). In what follows, an *example* is defined as the feature vector at a voxel in the training dataset, with its associated classification; a weak learner classifies example voxels as belonging to the hippocampus or not belonging to the hippocampus. When classifying an example, a weak learner gives a binary output value of +1 for example voxels that it regards as positive (i.e., in the hippocampus) and −1 for example voxels it regards as negative (i.e., outside the hippocampus).

Fig. 1 gives an overview of the AdaBoost algorithm. In our implementation, labeling the hippocampus is formulated as a two-class classification problem, in which the training data consists of input vectors of features, $x_1...x_N$, also called *examples*, and associated labels, $y_i$. The components of the features are the outputs of the Haar filters, intensity measures, positions, and other feature detectors detailed earlier. The training phase of AdaBoost attempts to find the best combination of classifiers. Each data point, or example, is initially given a weight, $D_1(i)$. The weighting parameter for each data point is initially set to $1/N$ for all data points.

At this point, the construction of the set of weak learners $h_j$ (of size $J$) needs to be defined. We define a weak learner to be any feature, a threshold, and a boolean function representing whether or not observations above that threshold are positive (belong to the ROI) or negative (do not belong to the ROI). Therefore, our weak learner selects the feature that best separates the data into positive and negative examples given $D_t$. In order to do this, two histograms are constructed for each feature based on $D_t$, one that is only the positive examples, and another that is only the negative examples, these are then normalized and converted into cumulative distribution functions (CDFs). Finally, the threshold that minimizes the error based on these CDFs is chosen, and the lowest error over all features determines which weak learner is selected.

More formally, as detailed in Fig. 1, at each stage $t$ of the algorithm ($t=1$ to $T$), AdaBoost trains a new weak learner in which the weighting coefficients, $D_t(i)$, on the example data points are adjusted to give greater weight to the previously misclassified data points. In Fig. 1, $\varepsilon_j$ is the total error of the $j$th weak learner, determined by counting up all the examples misclassified, $1(y_i \neq h_j(x_i))$, weighted by their current weights at time $t$, $D_t(i)$. As such, they are weighted measures of the error rates of the weak learners. The best weak learner for stage $t$ is the one with the lowest error, $\varepsilon_t$. This learner is based on a feature that is most "independent" of the previous learners. The best weak learner at each step is chosen from the full set of weak learners, not just from the new ones computed in successive steps by AdaBoost. The coefficient $\alpha_t = (1/2) \log((1-\varepsilon_t)/\varepsilon_t)$ is defined to be a weighting coefficient for the $t$-th weak learner, which favors learners with very low error. The key to AdaBoost is that the influence of each example in the training set is re-weighted using the following rule: $D_{t+1} = D_t \exp(-\alpha_t y_i h_t(x_i))/Z_t$, with $Z_t$ a normalizer defined in Fig. 1, chosen so that the $D_{t+1}(i)$ will be a probability distribution, i.e., sum to 1 over all examples $x_i$. This re-weighting emphasizes examples that were wrongly labeled at the prior iteration. Successive classifiers are therefore forced to prioritize examples that were incorrectly classified, and these data points receive increasing priority, $D_t(i)$. The formula for $\alpha_t$ is chosen such that it is the unique $\alpha_t$ that minimizes $Z_t$ analytically, by satisfying $dZ_t(\alpha_t)/d\alpha_t = 0$; picked in this way $\alpha_t$ is guaranteed to minimize $Z_t$. The final vote $H(x)$ is based on a thresholded weighted sum of all weak learners (Fig. 1).

Because of the large number of examples to be classified, instead of using AdaBoost just once, a cascade was created, where at each node in the cascade examples that are clearly negative are discarded (a probability below 0.1). This allows the classifier to use different features for examples that are difficult to classify. The value of 0.1 was chosen because it was empirically shown to give good results in our other studies (Morra et al., 2007).

*Probabilistic interpretation*

Friedman et al. (2000) noted that the update rule for weights (the "boosting" steps) in AdaBoost can be given a probabilistic interpretation, i.e. it can be derived by assuming that the goal is to sequentially minimize an exponential error function. Given a linear combination of weak learners $f(\overrightarrow{x}) = \sum_{t=1}^{T} \alpha_t h_t(\overrightarrow{x})$, then the exponential error of a mislabeling may be defined as $E = \sum_{n=1}^{N} \exp(-y_n f_y(\overrightarrow{x_n}))$, where $y_i$ are the training set target values. If we wish to minimize $E$ by optimizing the weak learner $h_t(\overrightarrow{x})$, then it can be shown that the best re-weighting of the examples is given by the update rule for $D_{t+1}(i)$ (Friedman et al., 2000). Two comments are necessary: first, other AdaBoost variants have proposed altering the exponential error function, which AdaBoost minimizes, to be the cross-entropy, which is the log-likelihood of a well-defined probabilistic model and generalizes to the case of $K>2$ classes (Friedman et al., 2000); and second, if the exponential error function is used, AdaBoost will find its variational minimizer over all the functions in the span of the weak learners. In fact, AdaBoost iteratively seeks a minimizer of the expected exponential error

$$E_{x,y}(\exp(-yH(\overrightarrow{x}))) = \sum_{\text{all } y_i} \int \exp(-yH(\overrightarrow{x}))P(y|\overrightarrow{x})P(\overrightarrow{x})d\overrightarrow{x}$$

and arrives at the final classification by constrained minimization. Although minimization of the number of classification errors may seem like a better goal, in general the problem is intractable (Hoffgen and Simon, 1992), so it is conventional to minimize some other nonnegative loss function such as E. The process of selecting $\alpha_t$ and $h_t(\overrightarrow{x})$ may be interpreted as a single optimization step minimizing the upper bound on the empirical error; improvement of the bound is guaranteed, so long as $\varepsilon_t < 1/2$, and choosing $h_t$ and $\alpha_t$ in this way results in the greatest decrease in the exponential loss, in the space of weak learners, and converges to the infimum of the exponential loss (Collins et al., 2002).

Also, traditionally, AdaBoost does not define the $P(\overrightarrow{x})$ term, and just uses the sign of $f(\overrightarrow{x})$ as the strong learner. However, when using ACM, it is necessary that the output not be a decision rule, but rather a value in the range [0 1] representing the confidence that the

Given: $N$ labeled training examples $(\overrightarrow{x_i}, y_i)$ with $y_i \in \{-1, +1\}$ and $\overrightarrow{x_i} \in \mathbb{R}^M$ (we assume each $\overrightarrow{x_i}$ is of length $M$), a set of $J$ weak learners $h_j \in W$, and an initial uniform distribution of weights $D_1(i)$ over the examples
For $t = 1, ..., T$ :
- $\varepsilon_j = \sum_{i=1}^{N} D_t(i) 1(y_i \neq h_j(\overrightarrow{x_i}))$
- $[h_t, \varepsilon_t] = \arg \min_{h_j \in W} \varepsilon_j$
- Set $\alpha_t = \frac{1}{2} \log((1-\varepsilon_t)/\varepsilon_t)$
- Set $D_{t+1}(i) = D_t(i) exp(-\alpha_t y_i h_t(\overrightarrow{x_i}))/Z_t$
  $Z_t = 2\sqrt{\varepsilon_t(1-\varepsilon_t)}$, a normalization factor

In order to evaluate a new example $(\overrightarrow{x})$ we do the following:
$f(\overrightarrow{x}) = \sum_{t=1}^{T} \alpha_t h_t(\overrightarrow{x})$
$P(\overrightarrow{x}) = 1/(exp(-f(\overrightarrow{x})) + 1)$
$H(\overrightarrow{x}) = \begin{cases} 1 & (P(\overrightarrow{x}) > 0.5) \\ 0 & (P(\overrightarrow{x}) < 0.5) \end{cases}$

**Fig. 1.** An overview of the AdaBoost algorithm. 1 is an indicator function, returning 1 if the statement is true and 0 otherwise.

given example is positive or negative. Therefore, we employ the LogOdds transform (Pohl et al., 2007) to map the interval $(-\infty\ \infty)$ to $(0\ 1)$. The LogOdds transform essentially makes the optimal classifier produce Bayesian maximum likelihood estimates of the labeling, under the premise of using an exponential loss function.

As noted by Collins et al. (2002), instead of using $f(\vec{x})$ as a classification rule, one can consider that the $y_i$ are generated through a generative probability law, using $f(\vec{x})$ to estimate the probability of the associated label $y_i$. A common way to do this is to pass $f(\vec{x})$ through a logistic function, and use the estimate $P(y = \pm 1 | \vec{x}) = 1/(1 + \exp(-f(\vec{x})))$. The likelihood of the labels occurring in the training set is then $\prod_{i=1}^{N} 1/(1 + \exp(-y_i f(\vec{x})))$. Maximizing this likelihood is equivalent to minimizing the log loss of this model $\sum_{i=1}^{N} \ln(1/(1 + \exp(-y_i f(\vec{x}))))$.

### Auto context model

According to Bayesian theory, the goal of pattern recognition algorithms is to correctly model the posterior distribution defined as $P(y = \pm 1 | x) = P(x | y = \pm 1) P(y = \pm 1) / P(x)$. AdaBoost itself may be regarded as providing an approximation to this probability (Shi et al., 2005), and since we are using a shape prior, AdaBoost models the combination of the conditional and prior probabilities (the marginal probability is a constant). In the simplest case, Bayes' rule looks at each example independently of all others. However, in our case, and in fact in most image segmentation cases, the posterior distribution of nearby voxels should influence each other. In any pattern recognition algorithm that attempts to model the Bayesian posterior, this information is mostly ignored, although some Markov methods have been proposed that make use of empirically estimated prior distributions on the joint labeling of contiguous voxels (Fischl et al., 2001). Here, we include this information by modeling $P(y = \pm 1 | x, x_{\text{neighbors}}) = P(x, x_{\text{neighbors}} | y = \pm 1) P(y = \pm 1) / P(x, x_{\text{neighbors}})$.

ACM attempts to model the above distribution iteratively; a description is given in Fig. 2.

In our context, $H$ is the cascade of AdaBoosts without the final binary classification step. In order to improve ACM, instead of starting $P_1$ with a uniform distribution, we instead start with our shape prior. Also, in order to give more information about the classifications of neighboring voxels, when running AdaBoost inside of ACM, we included neighborhood features defined on $P_t$. Specifically we included the same Haar, curvature, gradient, mean, and standard deviation filters on the posterior map as we do on the images.

We can prove that for each iteration of ACM, the error is monotonically decreasing. Define the error of the classification algorithm (in our case a cascade of AdaBoosts) at iteration $t$ to be $\varepsilon_t$, we then prove that $\varepsilon_t \leq \varepsilon_{t-1}$. First, we define $p_t(y_i|x_i)$ to be the probability change associated with iteration $t$ of ACM. Next, since $P_{t-1}$ includes all previous iterations of ACM, we can write $\varepsilon_{t-1} = -\sum_{i=1}^{N} \log P_{t-1}(i) y_i$ and $\varepsilon_t = -\sum_{i=1}^{N} \log p_t(y_i|x_i, P_{t-1}(i))$. In the trivial case, $p_t(y_i|x_i, P_{t-1}(i)) = P_{t-1}(i) y_i$ by simply choosing $p_t$ to be a uniform distribution. However, since it has been shown that AdaBoost decreases the error at every iteration, it must choose weak learners that decrease $p_t$, therefore $\varepsilon_t \leq \varepsilon_{t-1}$.

Given: $N$ labeled images $(\vec{x_i}, y_i)$ with $y_i \in \{-1, +1\}$, a learning algorithm $H$, and a posterior distribution $P_1$
For $t = 1, \ldots, T$:
- $P_{t+1} = H(\vec{x_i}, P_t)$

$H(\vec{x}) = \begin{cases} 1 & (P(\vec{x}) > 0.5) \\ 0 & (P(\vec{x}) < 0.5) \end{cases}$

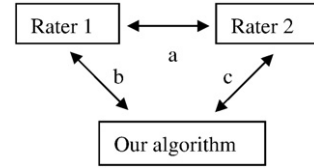Fig. 2. An overview of the auto context model.



Fig. 3. A schematic description of the comparisons performed. For all of the tests performed in this paper, training was performed on rater 1's tracings.

### Segmentation overview

When implementing our method there are a number of parameters that must be set, but very few that need to be tweaked. We used approximately 18,000 features in our feature pool. This includes both features based on the images, and those based on the posterior maps from ACM. We chose to run each AdaBoost for 200 iterations, obtaining 200 weak learners per AdaBoost cascade node, a cascade depth of two nodes, and five ACM iterations. This leads to running ten iterations of AdaBoost during the training phase. Overall, training takes about twelve hours. Even so, testing is very short, taking less than one minute to segment the hippocampus on a new brain image.

It is also of interest to note which features AdaBoost chose in order to obtain insight into the segmentation process. During the first iteration of ACM, AdaBoost chose mostly features based on the Haar filter and based on the tissue classified image (i.e., binary maps of gray and white matter and CSF). Later iterations of ACM chose mostly Haar filter outputs and mean filter outputs based on the previously selected posterior distribution, which means that neighboring voxels are influencing each other, as is to be expected. These features are not totally independent, since most are based on the same underlying image intensities; however each adds some classification ability to the final decision rule. An advantage of this approach is that the algorithm does not have to rely on the same small subset of features when trained on different training sets, and can select different features when trained on different examples, if they are optimal. As with other boosting methods, it is not expected or even desirable that the same feature sets be recovered when analyzing images from different sources, and it is not expected that each of the features used has good classification ability in its own right; in fact, any boosting method uses so-called "weak learners," with individual classification performance only slightly better than chance, and combines them effectively using the boosting strategy.

## Results

When validating a machine learning approach it is essential to examine error metrics on both the training and testing sets. A test set independent of the training set is vital in machine learning, in order to show the effectiveness of a classifier on data totally withheld from the training set. Since we used 21 hand-labeled brains to train the algorithm, we employed a leave-one-out analysis to guarantee a separation between the training and testing sets. In order to put our error metrics in context and decide whether they were acceptable for the application, we had a second independent expert rater trace the same 21 brains. We were then able to create a triangle of comparisons as shown in Fig. 3, in which the algorithm's segmentations can be compared with those of the human rater who trained the algorithm (rater 1; A.G.) and with those of an independent rater (rater 2; C.A.) who did not train the algorithm.

In order to show agreement with a human expert not involved with training the algorithm, we only trained our algorithm on manual segmentations from rater 1 and were still able to achieve good segmentation results that agreed well with rater 2's manual tracings. We emphasize that the validation against rater 1 is also an independent

**Table 2**
Precision, recall, relative overlap (R.O.), similarity index (S.I.), Hausdorff distance, and mean distance are reported for the training set (N=21)

|       | Precision | Recall | R.O. | S.I. | Hausdorff | Mean |
|-------|-----------|--------|------|------|-----------|------|
| Left  | 0.892     | 0.930  | 0.836 | 0.911 | 2.09 mm | 0.00262 mm |
| Right | 0.885     | 0.927  | 0.828 | 0.906 | 2.25 mm | 0.00299 mm |

Note that lower values are better for the Hausdorff distance and mean error (reported here in millimeters); higher values are better for the other metrics.

validation in the sense that our algorithm was classifying images that it was not trained on (i.e. a leave-one-out approach).

Secondly, we further validated our approach using volumetric results of three kinds. We hypothesized that hippocampal volume would decrease as the disease progresses further, and verified this by comparing mean volumes in groups of controls, MCI subjects, and AD patients. We also examined whether, in the full sample, hippocampal volume was correlated with clinical measurements of cognitive impairment; encouragingly, we found that measures from our segmentations correlated more strongly with cognition, in the hippocampus, than measures from a popular technique for quantification of brain atrophy, tensor-based morphometry, which is closely related to voxel-based morphometry.

Finally, since longitudinal follow-up scans were available for the individuals tested in this paper, we used scans taken six months later to assess the longitudinal stability of the segmentations of the same subject. We showed that the amount of hippocampal volume change was consistent with prior reports in the literature.

*Error metrics*

To assess our segmentations' performance, we first define a number of error metrics based on the following definitions: A, the ground truth segmentation, and B, the testing segmentation. Additionally, we define $d(a,b)$ as the Euclidean distance between points $a$ and $b$.

- Precision $= \dfrac{A \cap B}{B}$
- Recall $= \dfrac{A \cap B}{A}$
- Relative Overlap $= \dfrac{A \cap B}{A \cup B}$
- Similarity Index $= \dfrac{A \cap B}{\left(\frac{A+B}{2}\right)}$
- $H_1 = \max_{a \in A} (\min_{b \in B} (d(a,b)))$
- $H_2 = \max_{b \in B} (\min_{a \in A} (d(b,a)))$
- Hausdorff $= \dfrac{H_1 + H_2}{2}$
- Mean $= \text{avg}_{a \in A} (\min_{b \in B} (d(a,b)))$

First, Table 2 presents our segmentation performance on the training set. For this analysis, we used all 21 brains as training data, and tested on all 21 brains. These performance results on the training set represent an upper bound for the expected accuracy on the testing set. Next, we used our leave-one-out approach to obtain testing

**Table 3**
Precision, recall, relative overlap (R.O.), similarity index (S.I.), Hausdorff distance, and mean distance are reported for the leave-one-out analysis (N=21) when the algorithm was trained on 20 segmentations from rater 1 and tested on a single independent segmentation from rater 1, for all possible selections of the independent segmentation, using a jack-knifing procedure

|       | Precision | Recall | R.O. | S.I. | Hausdorff | Mean |
|-------|-----------|--------|------|------|-----------|------|
| Left  | 0.845     | 0.882  | 0.757 | 0.860 | 2.85 mm | 0.00459 mm |
| Right | 0.845     | 0.867  | 0.744 | 0.852 | 3.56 mm | 0.00587 mm |

**Table 4**
Precision, recall, relative overlap (R.O.), similarity index (S.I.), Hausdorff distance, and mean distance are reported for the leave-one-out analysis (N=21) when trained on rater 1 and tested on rater 2

|       | Precision | Recall | R.O. | S.I. | Hausdorff | Mean |
|-------|-----------|--------|------|------|-----------|------|
| Left  | 0.860     | 0.863  | 0.754 | 0.859 | 3.08 mm | 0.00416 mm |
| Right | 0.833     | 0.848  | 0.719 | 0.835 | 3.82 mm | 0.00633 mm |

We note that the Hausdorff errors are only slightly higher than in Table 3, which is to be expected as these errors incorporate differences of opinion between the two human raters.

metrics comparing our results to rater 1 (leg "b" in Fig. 3), shown in Table 3. Table 4 compares our method with rater 2 (leg "c" in Fig. 3), again using the leave-one-out technique. Finally, we compared the two human raters directly with one another (leg "a" in Fig. 3) in Table 5.

The first thing to note is that the error metrics from the training and test sets are very close to each other, with the testing metrics being slightly worse than the training metrics (which is to be expected). This shows that ACM is not memorizing the data, but instead learning the underlying structure of the hippocampus. Next, our algorithm shows only a small difference in the error metrics as opposed to the difference between the two human raters. Specifically, if Tables 4 and 5 are compared, the relative overlap between two human raters is on average 74.9% for the left and 74.3% for the right hippocampus (Table 5), while the relative overlap between the algorithm and a rater not involved in training it was 75.4% for the left and 71.9% for the right hippocampus (Table 4). This shows that the errors in our algorithm are comparable to the differences between two raters. In terms of precision, the agreement between the two human raters is about 3% higher than the agreement between the algorithm and the rater not used to train it, with all values in the 83–89% range. For recall, the algorithm agrees with the 2nd rater at least as well as the 1st rater agrees with the 2nd rater, with all values in the 82–86% range. The only metric for which the human raters agree with each other more than they do with the algorithm is the mean error (see Tables 4 and 5), but for that metric agreement is very high between all three suggesting that any biases are very small.

To further compare the performance of our approach with other segmentation methods, in Table 6 we present error metrics from three other papers that report either fully or semi-automated hippocampal segmentations. We present these only to show that ours is within the same range as other automated approaches. Since each study uses a different set of scans, an exact comparison is not possible.

*Volumetric validation*

Fig. 4 shows an example brain from the test set, with the right and left hippocampi overlaid in yellow and green. There is good differentiation of the hippocampus from the surrounding amygdala, overlying CSF, and adjacent white matter, and the traces are spatially smooth, simply connected, and visually resemble manual segmentations by experts. This image was chosen at random from the test set,

**Table 5**
Precision, recall, relative overlap (R.O.), similarity index (S.I.), Hausdorff distance, and mean distance are reported between the two human raters (N=21)

|       | Precision | Recall | R.O. | S.I. | Hausdorff | Mean |
|-------|-----------|--------|------|------|-----------|------|
| Left  | 0.891     | 0.827  | 0.749 | 0.856 | 2.89 mm | 0.0000417 mm |
| Right | 0.862     | 0.844  | 0.743 | 0.852 | 3.09 mm | 0.0000605 mm |

We note that in all metrics except the mean error, the two human raters agree with each other about as well as they agree with the algorithm. The agreement between human raters could be considered as an upper limit on the achievable agreement between the same raters and any algorithm, even if it were possible for an algorithm to make no errors.

**Table 6**
This table reports hippocampal segmentation metrics for other semi- and fully automated approaches

| | Recall | R.O. | S.I. |
|---|---|---|---|
| Powell et al. (2008) (Left: N=5) | 0.82 | 0.72 | 0.84 |
| Powell et al. (2008) (Right: N=5) | 0.83 | 0.74 | 0.85 |
| Fischl et al. (2002) (Left: N=134) | N.A. | ~0.78 | N.A. |
| Fischl et al. (2002) (Right: N=134) | N.A. | ~0.80 | N.A. |
| Hogan et al. (2000) (Left: N=5) | N.A. | 0.7378 | N.A. |
| Hogan et al. (2000) (Right: N=5) | N.A. | 0.7578 | N.A. |

Our results compare favorably to those reported here. A complete comparison is not possible without testing performance on the same set of brains.

**Table 7**
Inter-rater $r$ when comparing the three sets of volumes

| | Left | Right | Mean |
|---|---|---|---|
| Rater 1–Us | 0.740** | 0.717** | 0.724** |
| Rater 2–Us | 0.694** | 0.709** | 0.699** |
| Rater 1–Rater 2 | 0.844** | 0.857** | 0.854** |

These volumes were obtained from the leave-one-out analysis so a realistic testing environment can be observed.

\*\* $p<0.01$.

and is representative of the segmentation accuracy obtainable on the test images.

Table 7 shows that the inter-rater $r$ (intraclass correlation) between the two raters' hippocampal volumes and the volumes obtained from our algorithm's segmentations are comparable. Although the inter-rater $r$ is lower when comparing our approach to either rater versus the difference between the two raters, the intraclass correlation is high, and, as expected, statistically significant on both sides. For all of the tests in Table 7, we trained the algorithm only on segmentations from rater 1, and this is one reason why there is a slightly higher correlation observed with rater 1 than with rater 2.

Next, we present a disease-based validation technique, based on the premise that a necessary but not sufficient condition for a valid classifier is that it differentiates group mean hippocampal volumes between AD, MCI and controls. Since it is well-known that reductions in hippocampal volume are associated with declining cognitive function (Jack et al., 1999), we showed that our method is accurately capturing known mean volumetric differences between subgroups of interest with different stages of dementia (controls, MCI, and AD). Due to the limited sample size

($N=21$), we pooled left and right hippocampal volumes together for some of these results. Volumetric summaries were computed using the segmentations obtained in the leave-one-out testing analysis.

Fig. 5 and Table 8 show that there is a sequential reduction in volume between controls, MCI, and AD subjects, consistent with many prior studies (Convit et al., 1997). This shows that the brain MRIs we are working with show the expected profile of volumetric effects with disease progression, and that the segmentation approach is measuring hippocampal volumes with low enough methodological error to differentiate the 3 diagnostic groups, at least at the group level, in a very small sample.

Table 9 shows strong and significant positive correlations between hippocampal volume and MMSE scores ($r=0.587$ for the average of the left and right hippocampal volumes; $p<0.01$), and with sum-of-boxes CDR scores, for both the left and right, and mean hippocampal volumes ($r=-0.642$ for the mean volume, $p<0.01$). Correlations are high (around 0.6) when the average of the left and right hippocampal volumes is measured, suggesting that the hippocampal volumes explain a significant proportion of the variation in clinical decline. Although these associations are known, it provides evidence that the classifier error is low enough to allow their detection in small samples. Each of these values is significant despite the very small sample size, further confirming that our method is capable of capturing disease-associated hippocampal degeneration.

In a previous cross-sectional study on the ADNI dataset, we used tensor-based morphometry (TBM) to analyze brain differences associated with different stages of disease progression (Hua et al., 2008). TBM is a method based on high-dimensional image registration, which derives information on regional volumetric differences from a deformation field that aligns the images. TBM and voxel-based morphometry (VBM (Ashburner and Friston, 2000)) are closely linked and each measures voxel-wise expansion (or contraction) of the brain as compared to a minimal deformation template, which represents the mean anatomy of the subjects (Lepore et al., 2007).
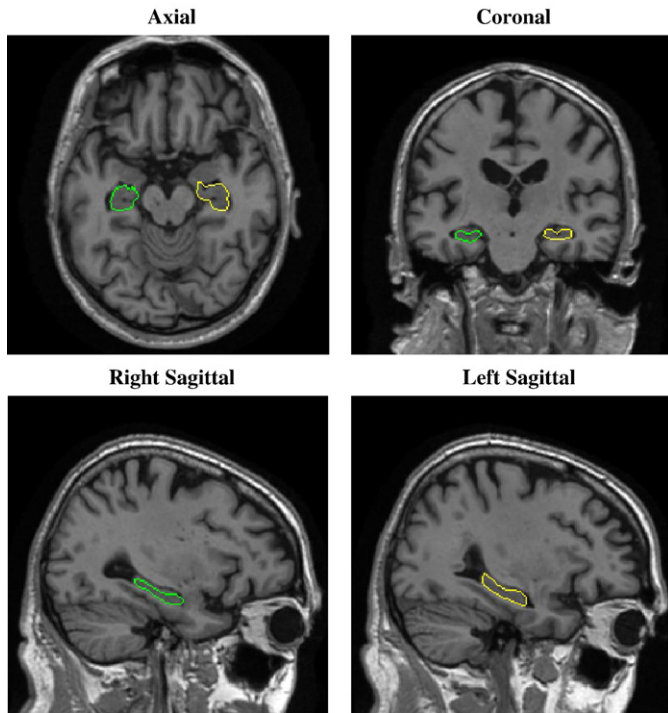


**Fig. 4.** Automated segmentation results for an individual from the testing set. Here the right hippocampus is encircled in yellow, and the left hippocampus in green. Axial, coronal, and two sagittal slices through the hippocampus show that the hippocampal boundary is captured accurately.
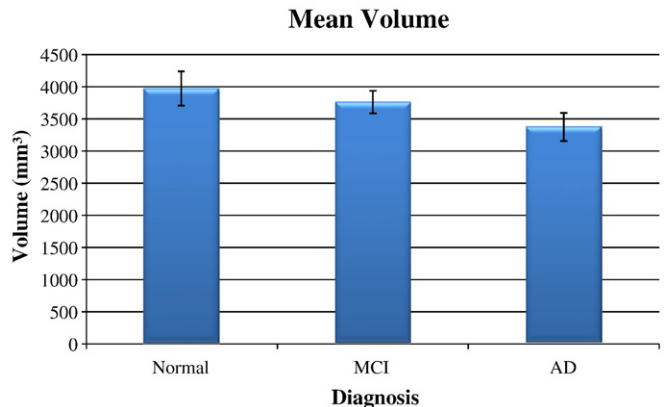


**Fig. 5.** Volumetric analysis for the three different diagnostic groups. The error bars represent standard errors of the mean. Percent differences are tabulated in Table 8.

**Table 8**
Mean differences in hippocampal volume (as a percentage) are shown for the groups listed in the left column for all subjects

|  | All |
|---|---|
| Normal–AD | 20.32%** |
| Normal–MCI | 4.13% |
| MCI–AD | 16.89%* |

Even though this is a very small sample (N=21; 7 of each diagnosis), there is a hippocampal volume reduction associated with declining function, and the group differences are significant even in a sample this small. These results are shown for validation purposes; a large sample in the future would allow more accurate estimation of deficits and factors that influence them.

 *$p < 0.05$.
 **$p < 0.01$.

Voxel-based morphometry (Davatzikos et al., 2001; Good et al., 2001) is a related approach that modulates the voxel intensity of a set of spatially normalized gray matter maps by the local expansion factor of a 3D deformation field that aligns each brain to a standard brain template.

Although TBM has proven useful in quantifying brain atrophy over time in 3D (Leow et al., 2005a; Studholme et al., 2004; Teipel et al., 2007), in cross-sectional studies TBM can be less effective for quantifying volumetric differences in small brain regions (such as the hippocampus) when the ROI is defined on the minimal deformation template.

This is to be expected, as TBM may be considered a rudimentary hippocampal segmentation approach that works by fluidly deforming a mean anatomical template onto the target image — the criteria to guide accurate segmentations are typically limited to measures of agreement in image intensities, such as the mutual information (Leow et al., 2005b; Viola and Wells, 1995). Table 10 shows the correlation between hippocampal volume (as measured with TBM) and MMSE and sum-of-boxes CDR scores. Note that none of the correlations is even significant in this small sample, and the measures compare poorly with those shown in Table 9. This suggests that our direct segmentation of hippocampal anatomy via voxel-level classification is better correlated with cognition than measures we previously obtained using a deformation-based morphometry method.

*Longitudinal validation by repeat scanning*

As a final validation approach, we segmented a set of six-month follow-up scans, acquired using an identical imaging protocol, for the individuals whose baseline scans were analyzed in this paper. At the time of writing, six-month follow-up scans were available for 18 of the 21 subjects analyzed in this paper, including 6 AD patients, 5 MCI patients, and 7 control subjects. Due to the very small sample size (especially in the AD and MCI groups) and short interval, we present this analysis to show that our algorithm is reproducible, giving relatively consistent hippocampal volumes over a short

**Table 9**
This table reports the correlations between hippocampal volumes and clinical covariates

|  | Left HP volume | Right HP volume | Mean HP volume |
|---|---|---|---|
| MMSE | 0.423* | 0.579** | 0.587** |
| Sum-of-boxes CDR | −0.369* | −0.705** | −0.642** |

A desirable but not sufficient condition for a hippocampal segmentation approach is that the methodological error is small enough for correlations to be detected between cognition and hippocampal volume. As expected, correlations are positive between MMSE scores and hippocampal volume, as higher MMSE scores denote better cognitive performance. Also as expected, correlations are negative between hippocampal volume and sum-of-boxes CDR, as higher CDR scores denote more severe impairment.

 *$p < 0.05$.
 **$p < 0.01$.

**Table 10**
This table reports the correlations between hippocampal volumes estimated using tensor-based morphometry (as reported (Hua et al., 2008)) and clinical covariates on the hippocampus when using TBM

|  | Left HP expansion | Right HP expansion | Mean HP expansion |
|---|---|---|---|
| MMSE | 0.099 | 0.143 | 0.126 |
| Sum-of-boxes CDR | −0.151 | −0.272 | −0.153 |

None of these correlations has a significant $p$-value, by contrast with the hippocampal volume measures obtained by our algorithm, which correlate strongly with cognitive and clinical decline (Table 9).

interval, when minimal hippocampal volume loss is expected. Table 11 shows that there is minimal loss over 6 months, which is to be expected. We note that this change represents a combination of biological changes and the methodological errors in segmentation, which derive partly from the algorithm and partly from the fact that the image acquisition is not perfectly reproducible. As these sources of methodological error are expected to be small and additive, the fact that the mean change is near 1.5% for the left and 0% for the right hippocampus is in line with expectation. Given that some small biological change is also occurring, this suggests good longitudinal stability for the volume measurements obtained by our algorithm.

## Discussion

In this study, we have demonstrated that ACM is an effective method for segmenting the hippocampus. There were three major findings. First, the agreement between our algorithm and two different human raters was comparable with their agreement with each other, which is a reasonable target for segmentation accuracy given that even trained human raters do not entirely agree on the labeling of all hippocampal voxels. Second, we found that the agreement with a rater not involved with training the algorithm was almost as good as the agreement with the rater who trained it, suggesting acceptable inter-rater reliability versus expert human raters. Third, we found that the hippocampal volumes segmented by our algorithm correlated well with cognitive and clinical ratings of dementia severity, which is an important characteristic for an automated volume measurement algorithm. For an algorithm to be useable in a drug trial context for the quantification of brain atrophy, it is necessary for the automatically measured volumes to replicate known differences in mean hippocampal volume between AD, MCI, and controls, and it is also desirable for the measures to be accurate enough to correlate with clinical measures of disease burden as they did here in a small sample (21 subjects; 7 of each diagnosis). In a further demonstration of longitudinal stability, we found that the change detected in 6-month repeat scans was around 0–1.5% for a group of 18 subjects. As this group was heterogeneous with regard to diagnosis and the time interval small, the intent of the experiment was merely to show that the mean changes were small, and within the range of expected biological variation.

**Table 11**
This table reports the % volume loss in the hippocampus for all 18 subjects that had follow-up scans over a 6-month interval

|  | Left HP | Right HP | Mean HP |
|---|---|---|---|
| % Loss | −1.47% | 0.08% | −0.01% |

For both hippocampi (and the mean volume), the mean percent loss is very small. This indicates good longitudinal reproducibility of our segmentation algorithm. For all of these tests, the $p$-value is greater than 0.3, indicating that there is no significant difference between baseline and 6 month follow-up hippocampal volumes. For this test we segmented the follow-up scans using the leave-one-out analysis so that a separation between training and testing brains at each time point is maintained.

This study is representative of several current research efforts that use automated methods to measure hippocampal atrophy in AD, including large diffeomorphic metric mapping (Csernansky et al., 2004; Wang et al., 2007), volumetric analysis (Geuze et al., 2005), and fluid registration (van de Pol et al., 2007). For purposes of comparison with our technique, we computed hippocampal volume measures from a related technique, known as tensor-based morphometry (TBM), which estimates anatomical structure volumes from a deformation transform that re-shapes a mean anatomical template onto each individual scan. Our TBM measures correlated poorly with cognitive assessments, although clearly in such a small sample the power to detect such associations is severely limited. Some reasons why TBM may not be optimal for hippocampal volumetric study are detailed in Hua et al. (2008) and Apostolova et al. (2006a); Becker et al. (2006); Frisoni et al. (2006). TBM is typically best for assessing differences at a scale greater than 3–4 mm (the typical resolution of the spectral representation used to compute the deformation field) (Hua et al., 2008; Leow et al., 2005a). For smaller-scale effects, direct modeling of the structure, e.g. using surface-based geometrical methods, may offer additional statistical power to detect sub-regional differences. Even then, it may not be possible to achieve accurate regional measurements of atrophy, especially in small regions such as the hippocampus, since that would assume a local highly accurate registration. Direct assessments of hippocampal volume by our ACM algorithm correlated better than TBM did with clinical dementia ratings and MMSE scores, and explained a substantial proportion of their variance even in this relatively small sample ($r \sim 0.6$; $p < 0.01$; $N = 21$). Conversely, a relative advantage of TBM, and other voxel-based mapping approaches, such as voxel-based morphometry, is that they map the profile of atrophy throughout the brain without the need for explicit segmentation of anatomical structures. VBM has been widely used in Alzheimer's disease studies, and does not rely on an explicit segmentation of hippocampal anatomy in each scan, other than that which is implied in a voxel-based analysis by aligning scans to a common template. Chetelat et al. (2005), for example, tracked gray matter loss with VBM in a longitudinal study of 18 MCI patients. Whitwell et al. (2007) demonstrated the profile of gray matter loss over three years in 63 MCI subjects, and Good et al. (2002) compared VBM to region-of-interest analysis and showed that they compared favorably in detecting structural differences in Alzheimer's disease.

The machine learning approach presented here selects features based on a training set of expert segmentations, so it may generalize well for segmenting other subcortical structures, such as the thalamus and basal ganglia. The next step will be to further examine ACM with AdaBoost by evaluating it on a large sample, and examining its performance on other subcortical structures.

## Acknowledgments

## References

Apostolova, L.G., Dinov, I.D., Dutton, R.A., Hayashi, K.M., Toga, A.W., Cummings, J.L., Thompson, P.M., 2006a. 3D comparison of hippocampal atrophy in amnestic mild cognitive impairment and Alzheimer's disease. Brain 129, 2867–2873.

Apostolova, L.G., Dutton, R.A., Dinov, I.D., Hayashi, K.M., Toga, A.W., Cummings, J.L., Thompson, P.M., 2006b. Conversion of mild cognitive impairment to Alzheimer disease predicted by hippocampal atrophy maps. Arch. Neurol. 63, 693–699.

Ashburner, J., Friston, K.J., 2000. Voxel-based morphometry—the methods. Neuroimage 11, 805–821.

Barnes, J., Scahill, R.I., Boyes, R.G., Frost, C., Lewis, E.B., Rossor, C.L., Rossor, M.N., Fox, N.C., 2004. Differentiating AD from aging using semiautomated measurement of hippocampal atrophy rates. Neuroimage 23, 574–581.

Becker, J.T., Davis, S.W., Hayashi, K.M., Meltzer, C.C., Toga, A.W., Lopez, O.L., Thompson, P.M., 2006. Three-dimensional patterns of hippocampal atrophy in mild cognitive impairment. Arch. Neurol. 63, 97–101.

Boyes, R.G., Gunter, J.L., Frost, C., Janke, A.L., Yeatman, T., Hill, D.L., Bernstein, M.A., Thompson, P.M., Weiner, M.W., Schuff, N., Alexander, G.E., Killiany, R.J., DeCarli, C., Jack, C.R., Fox, N.C., 2008. Intensity non-uniformity correction using N3 on 3-T scanners with multichannel phased array coils. Neuroimage 39, 1752–1762.

Chetelat, G., Landeau, B., Eustache, F., Mezenge, F., Viader, F., de la Sayette, V., Desgranges, B., Baron, J.C., 2005. Using voxel-based morphometry to map the structural changes associated with rapid conversion in MCI: a longitudinal MRI study. Neuroimage 27, 934–946.

Cockrell, J.R., Folstein, M.F., 1988. Mini-mental state examination (MMSE). Psychopharmacol. Bull. 24, 689–692.

Collins, D.L., Neelin, P., Peters, T.M., Evans, A.C., 1994. Automatic 3D intersubject registration of MR volumetric data in standardized Talairach space. J. Comput. Assist. Tomogr. 18, 192–205.

Collins, D.L., Schapire, R.E., Singer, Y., 2002. Logistic regression, AdaBoost and Bregman distances. Machine Learning 48, 253–285.

Convit, A., De Leon, M.J., Tarshish, C., De Santi, S., Tsui, W., Rusinek, H., George, A., 1997. Specific hippocampal volume reductions in individuals at risk for Alzheimer's disease. Neurobiology of Aging 18, 131–138.

Crum, W.R., Scahill, R.I., Fox, N.C., 2001. Automated hippocampal segmentation by regional fluid registration of serial MRI: validation and application in Alzheimer's disease. Neuroimage 13, 847–855.

Csernansky, J.G., Joshi, S., Wang, L., Haller, J.W., Gado, M., Miller, J.P., Grenander, U., Miller, M.I., 1998. Hippocampal morphometry in schizophrenia by high dimensional brain mapping. Proc. Natl. Acad. Sci. U. S. A. 95, 11406–11411.

Csernansky, J.G., Wang, L., Joshi, S.C., Ratnanather, J.T., Miller, M.I., 2004. Computational anatomy and neuropsychiatric disease: probabilistic assessment of variation and statistical inference of group difference, hemispheric asymmetry, and time-dependent change. Neuroimage 23 (Suppl. 1), S56–68.

Davatzikos, C., Genc, A., Xu, D., Resnick, S.M., 2001. Voxel-based morphometry using the RAVENS maps: methods and validation using simulated longitudinal atrophy. Neuroimage 14, 1361–1369.

Du, A.T., Schuff, N., Amend, D., Laakso, M.P., Hsu, Y.Y., Jagust, W.J., Yaffe, K., Kramer, J.H., Reed, B., Norman, D., Chui, H.C., Weiner, M.W., 2001. Magnetic resonance imaging of the entorhinal cortex and hippocampus in mild cognitive impairment and Alzheimer's disease. J. Neurol. Neurosurg. Psychiatry 71, 441–447.

Duda, D., Hart, P., Stork, D., 2001. Pattern Classification, 2nd ed. Wiley-Interscience.

Fischl, B., Salat, D.H., Busa, E., Albert, M., Dieterich, M., Haselgrove, C., van der Kouwe, A., Killiany, R., Kennedy, D., Klaveness, S., Montillo, A., Makris, N., Rosen, B., Dale, A.M., 2002. Whole brain segmentation: automated labeling of neuroanatomical structures in the human brain. Neuron 33, 341–355.

Folstein, M.F., Folstein, S.E., McHugh, P.R., 1975. "Mini-mental state". A practical method for grading the cognitive state of patients for the clinician. J. Psychiatr. Res. 12, 189–198.

Freund, Y., Schapire, R.E., 1997. A decision-theoretic generalization of online learning and an application to boosting. J. Comput. Sys. Sci. 55, 119–139.

Friedman, J., Hastie, T., Tibshirani, R., 2000. Additive logistic regression: a statistical view of boosting (with discussion and a rejoinder by the authors). Annals of Statistics 28, 337–407.

Frisoni, G.B., Sabattoli, F., Lee, A.D., Dutton, R.A., Toga, A.W., Thompson, P.M., 2006. In vivo neuropathology of the hippocampal formation in AD: a radial mapping MR-based study. Neuroimage 32, 104–110.

Geuze, E., Vermetten, E., Bremner, J.D., 2005. MR-based in vivo hippocampal volumetrics: 2. Findings in neuropsychiatric disorders. Mol. Psychiatry 10, 160–184.

Good, C.D., Johnsrude, I.S., Ashburner, J., Henson, R.N., Friston, K.J., Frackowiak, R.S., 2001. A voxel-based morphometric study of ageing in 465 normal adult human brains. Neuroimage 14, 21–36.

Good, C.D., Scahill, R.I., Fox, N.C., Ashburner, J., Friston, K.J., Chan, D., Crum, W.R., Rossor, M.N., Frackowiak, R.S., 2002. Automatic differentiation of anatomical patterns in the human brain: validation with studies of degenerative dementias. Neuroimage 17, 29–46.

Gunter, J., Bernstein, M., Borowski, B., Felmlee, J., Blezek, D., Mallozzi, R., 2006. Validation testing of the MRI calibration phantom for the Alzheimer's Disease Neuroimaging Initiative Study. ISMRM 14th Scientific Meeting and Exhibition.

Hoffgen, K.U., Simon, H.U., 1992. Robust trainability of single neurons. Proceedings of the Fifth Annual Workshop on Computational Learning Theory. Association for Computing Machinery, Pittsburgh, Pennsylvania, United States, pp. 428–439.

Hogan, R.E., Mark, K.E., Wang, L., Joshi, S., Miller, M.I., Bucholz, R.D., 2000. Mesial temporal sclerosis and temporal lobe epilepsy: MR imaging deformation-based segmentation of the hippocampus in five patients. Radiology 216, 291–297.

Hua, X., Leow, A.D., Lee, S., Klunder, A.D., Toga, A.W., Lepore, N., Chou, Y.Y., Brun, C., Chiang, M.C., Barysheva, M., Jack Jr., C.R., Bernstein, M.A., Britson, P.J., Ward, C.P., Whitwell, J.L., Borowski, B., Fleisher, A.S., Fox, N.C., Boyes, R.G., Barnes, J., Harvey, D., Kornak, J., Schuff, N., Boreta, L., Alexander, G.E., Weiner, M.W., Thompson, P.M., Alzheimer's Disease Neuroimaging Initiative, 2008. 3D characterization of brain atrophy in Alzheimer's disease and mild cognitive impairment using tensor-based morphometry. Neuroimage.

Hughes, C.P., Berg, L., Danziger, W.L., Coben, L.A., Martin, R.L., 1982. A new clinical scale for the staging of dementia. Br. J. Psychiatry 140, 566–572.

Jack Jr., C.R., Petersen, R.C., Xu, Y.C., O'Brien, P.C., Smith, G.E., Ivnik, R.J., Boeve, B.F., Waring, S.C., Tangalos, E.G., Kokmen, E., 1999. Prediction of AD with MRI-based hippocampal volume in mild cognitive impairment. Neurology 52, 1397–1403.

Jack, C.R., Jr., Bernstein, M.A., Fox, N.C., Thompson, P., Alexander, G., Harvey, D., Borowski, B., Britson, P.J., Whitwell, J.L., Ward, C., Dale, A.M., Felmlee, J.P., Gunter, J.L., Hill, D.L., Killiany, R., Schuff, N., Fox-Bosetti, S., Lin, C., Studholme, C., DeCarli, C.S., Krueger, G., Ward, H.A., Metzger, G.J., Scott, K.T., Mallozzi, R., Blezek, D., Levy, J., Debbins, J.P., Fleisher, A.S., Albert, M., Green, R., Bartzokis, G., Glover, G., Mugler, J., Weiner, M.W., 2008. The Alzheimer's Disease Neuroimaging Initiative (ADNI): MRI methods. J. Magn. Reson. Imaging 27, 685–691.

Jorm, A.F., Korten, A.E., Henderson, A.S., 1987. The prevalence of dementia: a quantitative integration of the literature. Acta. Psychiatr. Scand. 76, 465–479.

Jovicich, J., Czanner, S., Greve, D., Haley, E., van der Kouwe, A., Gollub, R., Kennedy, D., Schmitt, F., Brown, G., Macfall, J., Fischl, B., Dale, A., 2006. Reliability in multi-site structural MRI studies: effects of gradient non-linearity correction on phantom and human data. Neuroimage 30, 436–443.

Kantarci, K., Jack Jr., C.R., 2003. Neuroimaging in Alzheimer disease: an evidence-based review. Neuroimaging Clin. N. Am. 13, 197–209.

Leow, A., Huang, S.C., Geng, A., Becker, J., Davis, S., Toga, A., Thompson, P., 2005a. Inverse consistent mapping in 3D deformable image registration: its construction and statistical properties. Inf. Process Med. Imaging 19, 493–503.

Leow, A., Yu, C.L., Lee, S.J., Huang, S.C., Protas, H., Nicolson, R., Hayashi, K.M., Toga, A.W., Thompson, P.M., 2005b. Brain structural mapping using a novel hybrid implicit/ explicit framework based on the level-set method. Neuroimage 24, 910–927.

Leow, A.D., Klunder, A.D., Jack Jr., C.R., Toga, A.W., Dale, A.M., Bernstein, M.A., Britson, P.J., Gunter, J.L., Ward, C.P., Whitwell, J.L., Borowski, B.J., Fleisher, A.S., Fox, N.C., Harvey, D., Kornak, J., Schuff, N., Studholme, C., Alexander, G.E., Weiner, M.W., Thompson, P.M., 2006. Longitudinal stability of MRI for mapping brain change using tensor-based morphometry. Neuroimage 31, 627–640.

Lepore, N., Brun, C., Pennec, X., Chou, Y.Y., Lopez, O.L., Aizenstein, H.J., Becker, J.T., Toga, A.W., Thompson, P.M., 2007. Mean template for tensor-based morphometry using deformation tensors. Med. Image Comput. Comput. Assist Interv. Int. Conf. Med. Image Comput. Comput. Assist Interv. 10, 826–833.

Mazziotta, J., Toga, A., Evans, A., Fox, P., Lancaster, J., Zilles, K., Woods, R., Paus, T., Simpson, G., Pike, B., Holmes, C., Collins, L., Thompson, P., MacDonald, D., Iacoboni, M., Schormann, T., Amunts, K., Palomero-Gallagher, N., Geyer, S., Parsons, L., Narr, K., Kabani, N., Le Goualher, G., Boomsma, D., Cannon, T., Kawashima, R., Mazoyer, B., 2001. A probabilistic atlas and reference system for the human brain: International Consortium for Brain Mapping (ICBM). Philos. Trans. R. Soc. Lond. B. Biol. Sci. 356, 1293–1322.

McKhann, G., Drachman, D., Folstein, M., Katzman, R., Price, D., Stadlan, E.M., 1984. Clinical diagnosis of Alzheimer's disease: report of the NINCDS–ADRDA Work Group under the auspices of Department of Health and Human Services Task Force on Alzheimer's Disease. Neurology 34, 939–944.

Morra, J., Tu, Z., Apostolova, L.G., Green, A., Toga, A., Thompson, P., 2007. Comparison of AdaBoost and support vector machines for detecting Alzheimer's disease through automated hippocampal segmentation. IEEE Trans. Med. Imaging submitted.

Morris, J.C., 1993. The clinical dementia rating (CDR): current version and scoring rules. Neurology 43, 2412–2414.

Mueller, S.G., Weiner, M.W., Thal, L.J., Petersen, R.C., Jack, C., Jagust, W., Trojanowski, J.Q., Toga, A.W., Beckett, L., 2005a. The Alzheimer's Disease Neuroimaging Initiative. Neuroimaging Clin. N. Am. 15, 869–877 xi–xii.

Mueller, S.G., Weiner, M.W., Thal, L.J., Petersen, R.C., Jack, C.R., Jagust, W., Trojanowski, J.Q., Toga, A.W., Beckett, L., 2005b. Ways toward an early diagnosis in Alzheimer's disease: the Alzheimer's Disease Neuroimaging Initiative (ADNI). Alzheimers Dement. 1, 55–66.

Petersen, R.C., 2000. Aging, mild cognitive impairment, and Alzheimer's disease. Neurologic Clinics 18, 789–805.

Petersen, R.C., Smith, G.E., Waring, S.C., Ivnik, R.J., Tangalos, E.G., Kokmen, E., 1999. Mild cognitive impairment: clinical characterization and outcome. Arch. Neurol. 56, 303–308.

Petersen, R.C., Doody, R., Kurz, A., Mohs, R.C., Morris, J.C., Rabins, P.V., Ritchie, K., Rossor, M., Thal, L., Winblad, B., 2001. Current concepts in mild cognitive impairment. Arch. Neurol. 58, 1985–1992.

Pohl, K.M., Kikinis, R., Wells, W.M., 2007. Active mean fields: solving the mean field approximation in the level set framework. Inf Process Med Imaging 20, 26–37.

Powell, S., Magnotta, V.A., Johnson, H., Jammalamadaka, V.K., Pierson, R., Andreasen, N.C., 2008. Registration and machine learning-based automated segmentation of subcortical and cerebellar brain structures. Neuroimage 39, 238–247.

Quddus, A., Fieguth, P., Basir, O., 2005. Adaboost and support vector machines for white matter lesion segmentation in MR images. Conf. Proc. IEEE Eng. Med. Biol. Soc. 1, 463–466.

Shattuck, D.W., Sandor-Leahy, S.R., Schaper, K.A., Rottenberg, D.A., Leahy, R.M., 2001. Magnetic resonance image tissue classification using a partial volume model. Neuroimage 13, 856–876.

Shi, Y., Bobick, A., Essa, I., 2005. A Bayesian View of Boosting and Its Extensions. Georgia Tech's Institutional Repository, Georgia Institute of Technology.

Sled, J.G., Zijdenbos, A.P., Evans, A.C., 1998. A nonparametric method for automatic correction of intensity nonuniformity in MRI data. IEEE Trans. Med. Imaging 17, 87–97.

Studholme, C., Cardenas, V., Blumenfeld, R., Schuff, N., Rosen, H.J., Miller, B., Weiner, M., 2004. Deformation tensor morphometry of semantic dementia with quantitative validation. Neuroimage 21, 1387–1398.

Teipel, S.J., Born, C., Ewers, M., Bokde, A.L., Reiser, M.F., Moller, H.J., Hampel, H., 2007. Multivariate deformation-based analysis of brain atrophy to predict Alzheimer's disease in mild cognitive impairment. Neuroimage 38, 13–24.

Thompson, P.M., Hayashi, K.M., De Zubicaray, G.I., Janke, A.L., Rose, S.E., Semple, J., Hong, M.S., Herman, D.H., Gravano, D., Doddrell, D.M., Toga, A.W., 2004. Mapping hippocampal and ventricular change in Alzheimer disease. Neuroimage 22, 1754–1766.

Tu, Z., Narr, K.L., Dollar, P., Dinov, I., Thompson, P.M., Toga, A.W., 2008. Brain anatomical structure segmentation by hybrid discriminative/generative models. IEEE Trans. Med. Imaging 27, 495–508.

van de Pol, L.A., Barnes, J., Scahill, R.I., Frost, C., Lewis, E.B., Boyes, R.G., van Schijndel, R.A., Scheltens, P., Fox, N.C., Barkhof, F., 2007. Improved reliability of hippocampal atrophy rate measurement in mild cognitive impairment using fluid registration. Neuroimage 34, 1036–1041.

Viola, P., Jones, M.J., 2004. Robust real-time face detection. International Journal of Computer Vision 57, 137–154.

Viola, P., Wells, W.M., 1995. Alignment by maximization of mutual information. IEEE 16–23.

Wang, L., Beg, F., Ratnanather, T., Ceritoglu, C., Younes, L., Morris, J.C., Csernansky, J.G., Miller, M.I., 2007. Large deformation diffeomorphism and momentum based hippocampal shape discrimination in dementia of the Alzheimer type. IEEE Trans. Med. Imaging 26, 462–470.

Wechsler, D., 1987. Wechsler Memory Scale. Psychological Corp / Harcourt Brace Jovanovich, New York.

Whitwell, J.L., Shiung, M.M., Przybelski, S.A., Weigand, S.D., Knopman, D.S., Boeve, B.F., Petersen, R.C., Jack Jr., C.R., 2007. MRI patterns of atrophy associated with progression to AD in amnestic mild cognitive impairment. Neurology.

Yushkevich, P.A., Piven, J., Hazlett, H.C., Smith, R.G., Ho, S., Gee, J.C., Gerig, G., 2006. User-guided 3D active contour segmentation of anatomical structures: significantly improved efficiency and reliability. Neuroimage 31, 1116–1128.